ACS APPLIED MATERIALS & INTERFACES

Research Article

www.acsami.org

# Tuning the Photonic Stop Bands of Nanoporous Anodic Alumina-Based Distributed Bragg Reflectors by Pore Widening

Mohammad Mahbubur Rahman, Lluis F. Marsal, Josep Pallarès, and Josep Ferré-Borrull*

Nano-electronic and Photonic Systems (NePhoS), Departament d'Enginyeria Electrònica, Elèctrica i Automàtica, Universitat Rovira i Virgili, Avinguda Paisos Catalans 26, 43007 Tarragona, Spain

Supporting Information

**ABSTRACT:** A distributed Bragg reflector based on nanoporous anodic alumina was fabricated using an innovative cyclic anodization voltage approach, which resulted in an in-depth modulation of the pore geometry and the refractive index. The effect of a pore-widening wet-etching step on the structure's photonic stop-band properties was studied. From transmittance measurements, it was shown that by changing the pore-widening time it is possible to modulate the photonic stop band in the range of visible to near infrared. With the help of a theoretical model, we were able to obtain information about the evolution with the pore widening of the material effective refractive indexes. This opens the possibility of obtaining several optoelectronic devices based on nanoporous anodic alumina.

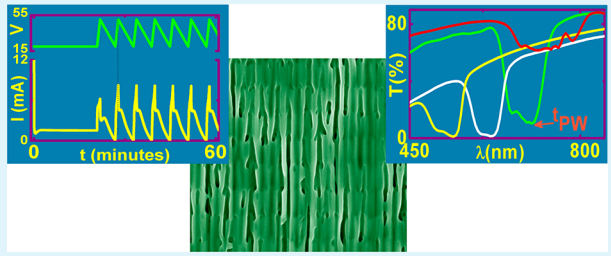


**KEYWORDS:** *nanoporous anodic alumina, distributed Bragg reflectors, optical properties, in-depth pore nanostructure*

## INTRODUCTION

The distributed Bragg reflector (DBR) is a multilayered structure that consists of periodically stacked layers with different refractive indexes. The main optical property of a DBR is that it can block light propagation in the direction perpendicular to the refractive index variation for a certain wavelength range, called the stop band.[1] The central wavelength of this stop band depends on the refractive index and thickness of the layers composing the DBR, whereas the stop-band width depends basically on the contrast between the refractive indexes and the relative thicknesses between the layers within one period, although it also depends on the total number of layers. DBRs are structures that can control the incident light (completely or partially) inside the material. This interesting photonic property makes DBRs potential candidates for the fabrication of various optoelectronic devices: light filters,[2] vertical cavity surface-emitting laser,[3,4] reflector mirrors,[5] electroabsorptive reflection modulators,[6] and others.

Nanoporous anodic alumina (NAA) is a self-assembled porous material with a 2D pattern having a characteristic interpore distance, which in some fabrication conditions can be on the order of the wavelength of visible light. It has been shown that it possesses stop bands for light propagating perpendicular to the pores.[7] This could lead to applications in sensing,[8−10] LED light extraction,[11] or laser-light generation.[12] Furthermore, it shows additional interesting properties such as a low absorption coefficient, excellent thermal stability,[13] wide electronic band gap (7−9.5 eV), and easy handling.

Recently, NAA-based DBR have been introduced in which refractive index variation is achieved with an in-depth varying porosity obtained with cyclic voltage profiles.[14−19] The authors proposed voltage profiles for one cycle consisting of a sinusoidal increasing voltage phase and two subsequent linear decreasing voltage phases with two different slopes. Wang et al.[15] fabricated nanoporous anodic alumina membranes (NAAM) with a band gap within the 450−525 nm range. Zheng et al.[18] reported a DBR based on periodic stacks of NAA layers obtained by the periodic modulation of the anodization voltage. With this, the first Bragg peak in the transmission spectra can be modulated between 727 and 1200 nm. Zheng also investigated the effect of temperature on NAA-based DBR with Bragg peaks that cover almost all wavelengths of visible light.[19] Other authors have also reported on the fabrication of complex pore architectures with modulated pore diameters by cycling between mild- and hard-anodization conditions,[16,17] although these works did not focus on the optical properties of the obtained nanostructures.

In a previous work, we have shown that when a pore-widening step is applied to NAA fabricated under different anodization voltages the porosity increases at a faster rate for the lower voltages. We also showed that the thickness depends linearly on the total charge spent in the anodization, regardless of the applied anodization voltage.[20] However, it is widely accepted that in the self-ordering regime of pore growth porosity depends weakly on the applied voltage.[21,22] Thus, if a cycling voltage is applied to obtain the NAA-based DBR, the different layers will have a small refractive index contrast and consequently poor stop-band characteristics. A subsequent

Received: October 1, 2013
Accepted: November 27, 2013
Published: November 27, 2013

  

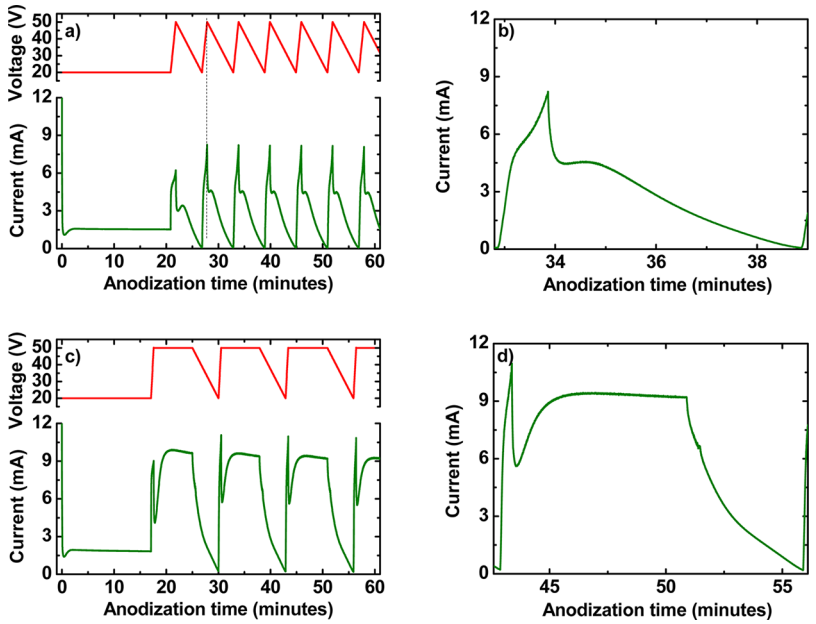


**Figure 1.** Applied voltage profiles (red) and measured current transients (green) for two different samples with $Q_0$ = 0 (top) and 4 C (bottom). (a, c) First hour of the anodization process. (b, d) Current transient of the third cycle. The dotted vertical line in panel a indicates that the time at which the anodization voltage reaches 50 V corresponds to the maximum of the current.

pore-widening step can increase such refractive index contrast and improve such characteristics.

In this work, we study the effect of the pore-widening step in the optical performance of a NAA-based DBR. To this end, we fabricated a NAA-based DBR by applying a simplified cyclic anodization voltage and we analyzed the evolution of their transmittance spectra with the pore-widening time. The voltage profile for one cycle consists of a linear increasing voltage phase followed by a constant voltage phase and then by a linear decreasing voltage phase. The analysis was performed on the basis of a theoretical model for the DBR, which permits information to be obtained on the evolution of the effective refractive indexes in the structure. We also analyzed the current transients in every cycle and field-emission scanning electron microscopy (FE-SEM) cross-sectional images to relate the current variations with the in-depth varying morphology of the pores. Although previous works have shown the possibility of obtaining DBR structures with NAA, to our knowledge, none of them has given evidence of the importance of the pore-widening step in the build up and tuning of the photonic stop bands as well as on its physical explanation.

## EXPERIMENTAL METHODS

We used high-purity Al substrates (99.999%) of 500 $\mu$m in thickness from Goodfellow Cambridge Ltd. The fabrication process was carried out by the following steps: (i) a pretreatment meliorated the physical properties of the commercial Al substrate, (ii) a first anodization step was performed to obtain self-ordered concavities on the electropolished aluminum, (iii) a newly designed cyclic anodization process was carried out in the second anodization step to obtain in-depth variations of the NAA structure, (iv) a wet-etching step to enlarge the pores followed, and finally, (v) the back aluminum was removed to enable optical transmittance measurements. In this section, the experimental details of these processes are given.

The physical properties of the NAA film were improved by a pretreatment process: first, the Al substrates were rinsed in deionized water, cleaned with ethanol, rinsed again in water, dried with $N_2$, and stored in a dry environment. Then, the surface roughness was reduced by an electropolishing process performed at room temperature and at 20 V for 4 min in a 1:4 v/v mixture of perchloric acid and ethanol. The sense of the stirrer was switched every 1 min. After electropolishing, the samples were cleaned in water. After the pretreatment, a first anodization was performed on the electropolished Al surface using a 0.3 M oxalic acid ($H_2C_2O_4$) solution at a temperature between 5 and 7 °C. The process was carried out at a constant voltage (V) of 40 V for 20 h. The resulting nanostructure after this first anodization step is a thin film of alumina with disordered pores at the top but self-ordered pores at the bottom.[23] This alumina film was dissolved by wet chemical etching at 70 °C in a solution of chromic and phosphoric acid (0.4 M $H_3PO_4$ and 0.2 M $H_3CrO_3$) stirred at 300 rpm for 4 h.

After the first anodization step, the second anodization step was carried out using the same acid electrolyte (0.3 M $H_2C_2O_4$) and the same temperature. The process starts at 20 V, and it lasts until a charge of 2 C has flowed through the system. In this way, a self-ordered layer of vertical pores is obtained. To obtain the DBR structure, after this anodization at 20 V, the cyclic anodization process starts immediately. Each cycle consists of three phases: (i) a linear increasing ramp from 20 to 50 V at a rate of 0.5 V/s, (ii) an interval of constant voltage at 50 V lasting for enough time to flow a given charge, $Q_0$, through the system, and (iii) a subsequent linear decreasing ramp from 50 to 20 V at 0.1 V/s (see Supporting Information Figure S1 for more details on the choice of the voltage ramp rates). Finally, after 150 cycles, a final anodization period at 20 V and lasting until 2 C are spent is applied. Four samples with four values of charge spent in phase ii, $Q_0$ = 0, 0.5, 1, and 4 C, were fabricated.

The anodizations were carried out in a PVC cell cooled by a circulating system (Thermo Scientific) with continuous stirring. The working surface area of the samples was 1.4 $cm^2$. A Pt grid was used as a cathode, and the distance between the two electrodes was about 2 cm. The electrochemical process was controlled through a software that registered the data of current, voltage, and the amount of charge flow through the system every 200 ms.

After the anodization process, the back Al substrate was removed. This process was carried out in a 1:4 v/v mixture of saturated solution of cupric chloride and hydrochloric acid ($CuCl_2$/HCl). Finally, a wet etching to increase pore radius (pore-widening step) was performed with 5 wt % phosphoric acid ($H_3PO_4$) at 35 °C. This pore widening was applied for different times (0, 9, 18, and 27 min). With this, samples were obtained for all of the range of pore widening times ($t_{PW}$) and $Q_0$, which are the variables of our study.

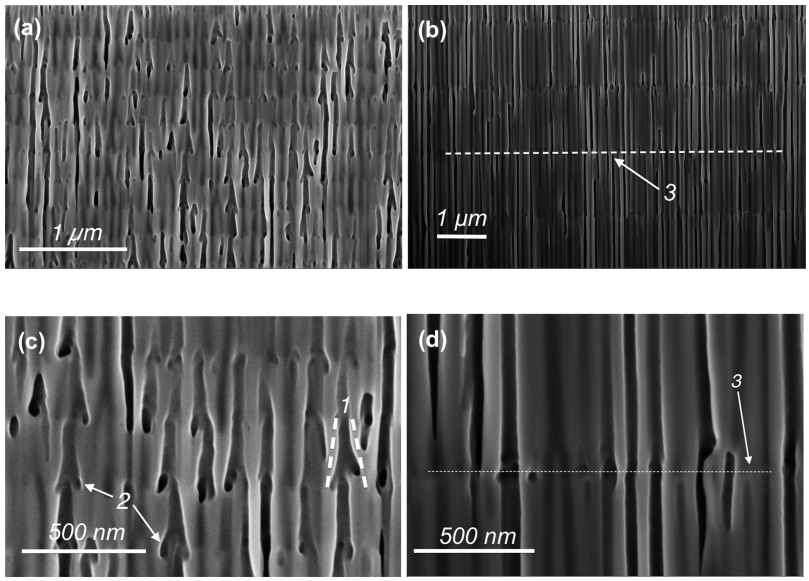


**Figure 2.** Cross-sectional FE-SEM images of DBR prepared with $Q_0$ = 0 (left) and 4 C (right). (a, b) Images showing several cycles. (c, d) Two images at exactly the same magnification. Conical shape of the pores is indicated by the label 1. The beginning of two branchings are indicated with label 2. Label 3 refers to interface between two cycles.

The NAA films were characterized by field-emission scanning electron microscopy (FE-SEM, Zeiss Neon 40). Direct transmittance measurements were carried at room temperature in the range from 300 to 2200 nm by a spectrophotometer (PerkinElmer, Lambda 950) with the incident light perpendicular to the NAA-based DBR. Diffuse transmittance were carried out in the range from 250 to 860 nm with the same spectrophotometer and a 150 mm integrating sphere. From the transmission spectra, the position of the central wavelength ($\lambda_0$) and stop-band width were estimated using a fitting procedure (see details in the Supporting Information, Figure S2). To detect changes in alumina composition, FTIR transmittance spectra in the range from 4000 to 400 $cm^{-1}$ were carried out with a Bruker Vertex 70 spectrometer.

## RESULTS AND DISCUSSION

The applied voltage-time and obtained current-time transients for two of the samples are shown in Figure 1a–d. Figure 1a,b corresponds to $Q_0$ = 0 C, whereas Figure 1c,d corresponds to $Q_0$ = 4 C. The first hour of the cyclic anodization step is shown in Figure 1a,c, whereas the third cycle is shown in more detail in Figure 1b,d. In the first part of the process corresponding to the constant voltage of 20 V, the current transient behaves like the second step in standard mild anodization for both the $Q_0$ = 0 and 4 C cases. This ensures the steady growth of the pores. Then, as the cyclic voltage is applied, the current transient describes a correspondingly cyclic behavior. With the increasing voltage ramp (phase i), the current increases until it reaches a peak when the voltage reaches the maximum value. The dotted vertical line in Figure 1a has been included to indicate that the time at which the anodization voltage reaches 50 V corresponds also to the maximum of the current. After this, with the beginning of the constant voltage phase (ii) the current shows a sudden decrease both for $Q_0$ = 0 and 4 C, until a minimum is reached and a current recovery is observed. In the sample with $Q_0$ = 4 C, the current in phase ii stabilizes in the same way as in the standard two-step process. With the decreasing voltage ramp (phase iii), the current decreases accordingly until a value near to 0 is reached.

A closer examination of the current behavior within one cycle shows that there exist different current regimes even within a phase. This can be seen in Figure 1b,d and also in Figure S3 in the Supporting Information. Figure S3a,b depicts the $V/I$ ratio in the third cycle of anodization for the same samples as in Figure 1. In Figure 1b,d, two regimes can be observed for the increasing voltage phase: a first regime where the current has a sharp increase and a second regime with a more moderate increase. This is more evident in the $V/I$ curves, where the first regime is indicated by a sharp decrease, and the second regime corresponds to an almost constant $V/I$ value. The constant voltage phase clearly shows also two regimes, which are equivalent to the two regimes observed in standard two-step anodizations: a first regime corresponding to a decrease until a minimum is reached and a subsequent recovery followed by a second stable regime. In the $V/I$ curve, this is indicated by a transient part in the curve followed by a stable $V/I$ value, which can be related to a constant barrier-layer thickness. Finally, two regimes also exist for the decreasing voltage phase: a first regime with an exponential-like decrease of the current followed by a linear decrease at a constant rate. In the $V/I$ curves, this is shown by a first regime with a linear increase followed by a faster nonlinear increase.

These two regimes observed in each phase could be explained on the basis of the dynamics of the barrier-layer thickness. It is commonly accepted[21] that in steady-state growth the barrier-layer thickness is proportional to the applied anodization voltage. Thus, the existence of two current regimes in each phase indicates the existence of two different barrier-layer thickness dynamics within each phase: a first transient regime followed by a more steady behavior. To clarify this concept, let us consider the end of the constant voltage phase in which the current is constant, which corresponds to steady pore growth and a constant barrier-layer thickness. As the decreasing voltage phase begins, the current shows a sharp decrease, which indicates that the barrier layer still remains with the same thickness. After a given time, the decreased rate of the current becomes more steady, which can be explained by a decrease with time of the barrier-layer thickness to adjust to the new voltage value. Then, as the voltage begins to increase again, it follows the same trend: first, a transient regime in which the

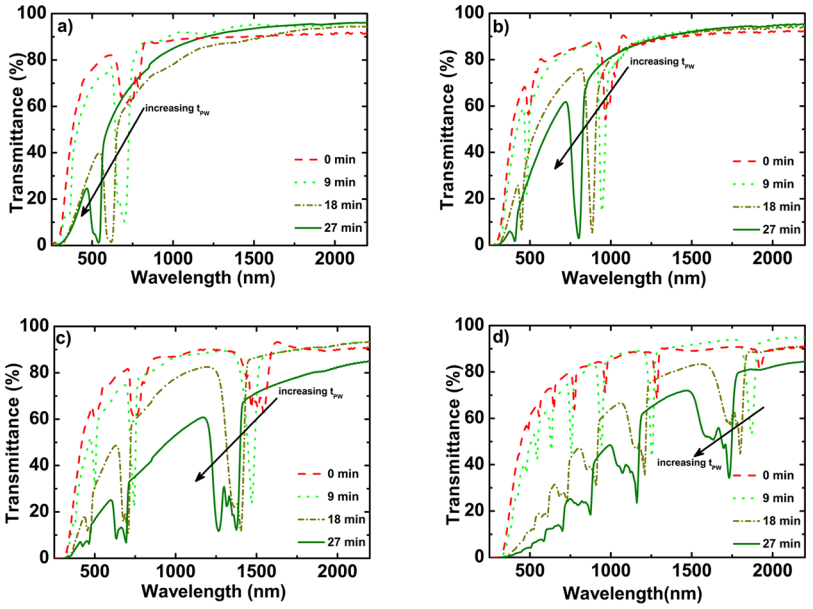


**Figure 3.** Transmittance spectra of the NAA-based DBR for different $Q_0$ and different pore-widening times. (a) $Q_0$ = 0 C, (b) $Q_0$ = 0.5 C, (c) $Q_0$ = 1 C, and (d) $Q_0$ = 4 C.

barrier layer is still becoming thinner in spite of the voltage increase (giving rise to a sharp increase in current), and second, a more moderate increase in current with voltage as the barrier-layer thickness begins to increase at a steady rate. These observations suggest that the barrier-layer thickness shows some kind of inertia in its dynamics.[24]

Figure 2a–d shows cross-sectional FE-SEM images of the as-anodized samples with $Q_0$ = 0 and 4 C. The top images correspond to cross sections where several cycles can be distinguished. The bottom images show cross-sectional pictures of the two samples on the same scale to enable a comparison of pore sizes and cycle thicknesses.

The pictures for the $Q_0$ = 0 C sample show cone-like pores (indicated by dashed lines labeled with 1) with the beginning of a branching at the edge between cycles (2). This pore branching indicates that such edge corresponds to the smallest voltage within the cycle, where the pore size and barrier-layer thickness should be the smallest. Pores for the $Q_0$ = 4 C sample are mainly cylindrical except at the cycle edge where branching is observed in some cases (3). This is expected because most of the charge spent in the process is used in the constant voltage phase.

Figure 3 shows the transmittance spectra of samples prepared for $Q_0$ = 0, 0.5, 1, and 4 C. Each graph contains the spectra corresponding to the different applied pore-widening times. The arrows indicate the evolution of the stop bands in the transmittance spectra with increasing pore-widening time. All of the spectra show stop bands, as expected in a cyclic structure. In all cases, the transmittance shows a general behavior of decreasing with decreasing wavelength, and below 320 nm, it is nearly zero (because bandgap absorption is dominant in this spectral range). Besides, the overall transmittance also decreases for increasing pore-widening times. This decrease in transmittance can be attributed to scattering losses produced by the irregular interfaces between cycles (which can be observed in the FE-SEM pictures in Figure 2) and by the roughness of the top and bottom surfaces of the samples. To confirm this assumption, diffuse transmittance measurements were performed for the sample with $Q_0$ = 1 C for the different pore-widening times. The results are included in Figure S4 of the Supporting Information. These results show a difference between diffuse transmittance and direct transmittance in the range from 250 to 860 nm, and it can be observed that this difference increases with increasing $t_{PW}$. In addition to these diffuse reflectance measurements, transmission FTIR measurements were performed for the same samples and for the different $t_{PW}$. The resulting spectra are included in Figure S4 of the Supporting Information, and it can be noticed that all of the spectra show the same behavior. This demonstrates that the pore-widening process has no effect on NAA composition. This together with the increasing amount of scattered light in the transmission demonstrates that losses in these structures are mainly due to scattering, as mentioned earlier. The pore-widening process tends to increase such irregularities and roughness, giving rise to the losses. Another feature that can be observed in the graphs in Figure 3 is that the transmittance in the spectral ranges between stop bands is the same regardless the $Q_0$. This indicates that the total thickness of the NAA layer does not influence the overall sample transmittance.

By examining the stop bands in the spectra, there is a clear difference between the stop bands observed for the as-produced samples and the samples after the pore widening: the transmittance within the stop band for the samples after pore widening shows a smoother behavior and a lower minimum value than the same stop bands for the as-anodized samples. This can be explained by the small differences in the refractive indexes for nanoporous anodic alumina produced with slightly different voltages in the same electrolyte type and concentration and at the same temperature.[20,21] Thus, in the as-anodized samples, even though the morphology of the pores changes with voltage, the overall porosity and refractive index does not substantially vary as the pores evolve. Consequently, the differences in the refractive index within one anodization cycle are small, and the corresponding stop bands cannot block completely the light. However, for the samples after pore widening, it is known that the refractive index contrast increases[20] at the expense of an overall decrease of the

refractive index absolute value, which results in stop bands shifted to lower central wavelengths.

The central wavelength ($\lambda_0$) of the stop bands shifts to lower values as the pore-widening time increases. The dependence of the estimated experimental central wavelength with the pore-widening time and with the total charge spent in the constant voltage phase, $Q_0$, is plotted in Figure 4 (error bars). These data

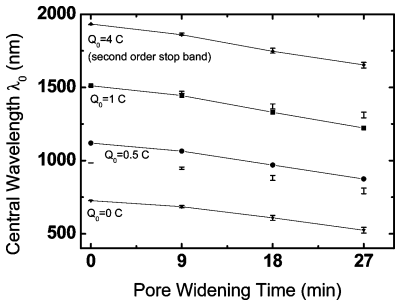


**Figure 4.** Evolution of the estimated stop-band central wavelength with the pore-widening time. Error bars correspond to the estimated experimental values and the corresponding standard deviation for the different $Q_0$ indicated in the graph. Closed symbols (linked with lines, included as a guide to the eye) correspond to the theoretically predicted values.

correspond to the first-order stop band for the samples with $Q_0$ = 0, 0.5, and 1 C, whereas for the sample with $Q_0$ = 4 C, the second-order stop band is represented because the first-order stop band is out of the measurement range. The amplitude of the error bars corresponds to the standard deviation estimated from four different samples for each $Q_0$ obtained under the same conditions. It is worth noting that the dispersion of $\lambda_0$ for the as-produced samples is as small as 0.7 nm and that this dispersion increases with the pore-widening time (up to 19 nm) for the samples with $t_{PW}$ = 27 min.

The graph includes the central wavelength values obtained from a theoretical model in which each cycle in the DBR is represented by two uniform layers: the first corresponding to the union of the increasing and decreasing voltage phases and the second to the constant voltage phase. The layers are considered uniform: the refractive index is constant and corresponds to an effective-medium[25] model. From FE-SEM pictures such as those in Figure 2 for the sample with $Q_0$ = 0 C, the overall average physical thickness of the increasing and decreasing voltage phases ($d_{ID}$) can be estimated. Because this thickness depends on the amount of charge spent in these phases and because this amount is similar for all of the fabricated samples, it can be assumed that this thickness is the same for all of the samples. In addition, from the FE-SEM pictures, the total thickness of one cycle for $Q_0$ = 4 C ($d_{TOTAL}$) can be estimated and hence the thickness corresponding to the 50 V constant voltage phase: $d_{50\ V} = d_{TOTAL} - d_{ID}$. Using these two estimated thicknesses, the thickness, $d_{50\ V}$, for the samples with different $Q_0$ can be predicted in a first approximation by assuming a linear proportion to the total charge spent in such phase: $d_{50\ V} = r_{50\ V}\ Q_0$, where $r_{50\ V}$ is the proportionality constant. In addition, the effective refractive index of the two layers can be estimated from the central wavelength of the samples with $Q_0$ = 0 and 4 C through the relation

$$d_{ID}n_{ID} + r_{50\ V}Q_0n_{50\ V} = \frac{\lambda_0}{2} \quad (1)$$

where $n_{ID}$ is the effective refractive index for the layer corresponding to the increasing and decreasing voltage phases, and $n_{50\ V}$ is the effective refractive index of the constant voltage phase layer. The estimated values of $r_{50\ V}$, $d_{ID}$, $n_{ID}$, and $n_{50\ V}$ for the different pore-widening times are reported in Table 1. With

**Table 1. Refractive Index and Thickness Values Estimated from the Data of Samples with $Q_0$ = 0 and 4 C That Were used to Obtain the Central Wavelengths in Figure 4**

| $t_{PW}$ (min) | $n_{50\ V}$ | $n_{ID}$ |
|---|---|---|
| 0 | 1.45 | 1.46 |
| 9 | 1.41 | 1.42 |
| 18 | 1.33 | 1.27 |
| 27 | 1.29 | 1.07 |
| $d_{IU}$ = 251 nm | | |
| $r_{50\ V}$ = 269 nm/C | | |

this model, the central wavelength for the samples with $Q_0$ = 0.5 and 1 C can be predicted using eq 1. From Figure 4, it is remarkable that this simple model shows a good agreement with the observed central wavelength values for these samples. These results indicate a good evaluation of the refractive indexes, $n_{ID}$ and $n_{50\ V}$, and of the thicknesses, $d_{ID}$ and $r_{50\ V}$.

Another feature that can be observed in the spectra of Figure 3 is the evolution of the stop-band width. The width does not follow a clear trend. In general, the stop-band width for the as-anodized samples is larger than the width for the corresponding samples with 9 min of pore-widening time except for the $Q_0$ = 4 C as-anodized sample, which shows comparatively narrow and shallow stop bands.

This behavior of the stop bands cannot be predicted by the two-layer model discussed earlier, especially for the as-anodized samples and for the samples with $t_{PW}$ = 9 min, where the refractive index contrast between $n_{ID}$ and $n_{50\ V}$ is rather small. This suggests that the actual refractive index varies with the depth in a more complex way. Although it is out of the scope of this work to determine precisely the refractive index profile within one cycle, a more accurate model for the refractive index can be proposed. To explain the remarkably observed wide stop bands, the two-layer model should be refined to a three-layer model. The generalization consists of splitting the layer corresponding to the increasing and decreasing voltage phases into two uniform layers with thicknesses $d_I$ and $d_D$ and effective-medium refractive indexes $n_I$ and $n_D$, respectively. The thicknesses and refractive indexes must be such that the central wavelength predicted by the two-layer model is preserved and thus the corresponding term in eq 1 should be expanded accordingly

$$d_{ID}n_{ID} = d_In_I + d_Dn_D \quad (2)$$

Table 2 reports the measured stop-band widths and the corresponding values obtained with the three-layer model for the samples with $t_{PW}$ = 18 min. Table 3 shows the evolution of

**Table 2. Measured Stop-Band Widths and Corresponding Values Obtained with the Three-Layer Model for the Samples with $t_{PW}$ = 18 min**

| $Q_0$ (C) | measured stop-band width (nm) | calculated stop-band width (nm) |
|---|---|---|
| 0 | 90 | 92 |
| 0.5 | 96 | 123 |
| 1 | 167 | 125 |


dx.doi.org/10.1021/am4043118 | ACS Appl. Mater. Interfaces 2013, 5, 13375−13381

**Table 3. Measured Stop-Band Widths and Corresponding Values Obtained with the Three-Layer Model for the Samples with $Q_0$ = 1 C**

| $t_{PW}$ (min) | measured stop-band width (nm) | calculated stop-band width (nm) |
|---|---|---|
| 0 | 202 | 148 |
| 9 | 123 | 122 |
| 18 | 167 | 127 |
| 27 | 165 | 161 |

the stop-band width with the pore-widening time for the samples with $Q_0$ = 1 C. The calculation of the widths has been carried out using a 1D plane-wave expansion photonic crystal formalism.[26] These results show that three-layer model is able to predict the order of magnitude of the observed stop-band widths. Figure 5 depicts the corresponding evolution of the

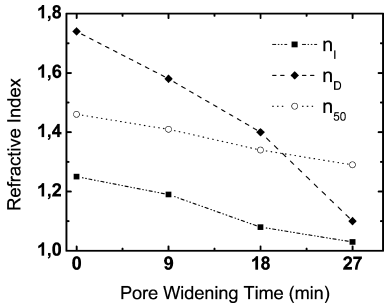


**Figure 5.** Values of the refractive indexes used in the three-layer model simulations.

refractive indexes used to obtain the values in Tables 2 and 3. It should be pointed out that the stop-band widths observed are systematically bigger than those predicted by the three-layer model, which suggests that the in-depth pore structure is more complex than the simple three-layer model.

## CONCLUSIONS

In this work, we show the influence of the pore-widening time on the optical properties of nanoporous anodic alumina-based distributed Bragg reflectors fabricated with a cyclic voltage anodization procedure. We show that it is possible to obtain DBR structures using a simplified voltage cycle as compared with previous work. Here, once cycle is composed of a linearly increasing voltage ramp followed by a constant voltage phase and a linearly decreasing voltage ramp.

We studied the behavior of the current transients with respect the voltage changes in one cycle, and we have shown the existence of different current regimes in each of the increasing, decreasing, or constant voltage phases. The existence of these current regimes can be explained from the dynamic behavior of the barrier layer and by the inertia of this barrier layer to change its thickness. This permitted the structural features observed in FE-SEM images to be related with the different phases of the anodization cycle.

By controlling accurately the amount of charge spent in each cycle, the stop-bands position can be modulated from the UV to the near-infrared range in a reproducible manner. When applying a pore-widening step, the stop bands shift to lower wavelengths and modify their width and depth. With a two-layer model, it is possible to predict the central wavelength of the fabricated samples as a function of the charge and of the pore-widening time. Concerning the stop-band width, a three-layer model predicts the order of magnitude observed experimentally, although a more complex model would be necessary for better agreement.

Taking advantage of the photonic properties of the fabricated DBR, especially in the visible range of wavelengths, and of the developed models, it is possible to design functional devices such as filters, structures for improved LED light extraction, sensors, and others.

## ASSOCIATED CONTENT

### Supporting Information

Estimation of the voltage ramp rates. Description of the fitting method to extract the stop-band central wavelength and width from spectrophotometric measurements. Alternative representation of the current transients showing the existence of two current regimes within each voltage phase. Comparison of diffuse and direct transmittance measurement and of FTIR transmittance spectra corresponding to the same sample for increasing pore-widening times. This material is available free of charge via the Internet at http://pubs.acs.org.

## AUTHOR INFORMATION

### Corresponding Author

*E-mail: josep.ferre@urv.cat. Tel: +34977559632. Fax: +34977559605.

### Author Contributions

The authors contributed equally to this work.

### Notes

The authors declare no competing financial interest.

## ACKNOWLEDGMENTS

This work was supported by the Spanish Ministry of Economy and Competitiveness MICINN under grant TEC2012-34397 and by the Generalitat de Catalunya under grant AGAUR 2009 SGR 549.

## ABBREVIATIONS

NAA, nanoporous anodic alumina; DBR, distributed Bragg reflector; $Q_0$, charge spent in the 50 V phase of the cycle in the anodization process; $t_{PW}$, pore-widening time; $\lambda_0$, stop-band central wavelength

## REFERENCES

(1) López, C. *Adv. Mater.* **2003**, *15*, 1684−1704.
(2) Avrutina, E. A.; Gorfinkel, V. B.; Luryi, S.; Shore, K. A. *Appl. Phys. Lett.* **1993**, *63*, 2460−2462.
(3) Yoon, J.; Lee, W.; Thomas, E. L. *Nano Lett.* **2006**, *6*, 2211−2214.
(4) Chena, L.; Toweb, E. *Appl. Phys. Lett.* **2006**, *89*, 053125-1−053125-3.
(5) Yan, R. H.; Simes, R. J.; Coldren, L. A. *Appl. Phys. Lett.* **1989**, *55*, 1946−1948.
(6) Zheng, W. J.; Fei, G. T; Wang, B.; Zhang, L. D. *Nanoscale Res. Lett.* **2009**, *4*, 665−667.
(7) Maksymov, I.; Ferré-Borrull, J.; Pallarès, J.; Marsal, L. F. *Photonics Nanostruct.: Fundam. Appl.* **2012**, *10*, 459−462.
(8) Santos, A.; Balderrama, V. S.; Alba, M.; Formentín, P.; Ferré-Borrull, J.; Pallarès, J.; Marsal, L. F. *Adv. Mater.* **2012**, *24*, 1050−1054.
(9) Santos, A.; Macías, G.; Ferré-Borrull, J.; Pallarès, J.; Marsal, L. F. *ACS Appl. Mater. Interfaces* **2012**, *4*, 3584−3588.
(10) Macias, G.; Hernández-Eguía, L. P.; Ferré-Borrull, J.; Pallarès, J.; Marsal, L.F. *ACS Appl. Matter. Interfaces* **2013**, *5*, 8093−8098.

(11) Fu, X. X.; Zhang, B.; Kang, X. N.; Deng, J. J.; Xiong, C.; Dai, T.; Jiang, X. Z.; Yu, T. J.; Chen, Z. Z.; Zhang, G. Y. *Opt. Express* **2011**, *19*, A1104.
(12) Sokol, V.; Gaponenko, S.; Yakovtseva, V.; Litvinovich, G.; Prislopsky, S.; Lutich, A. *Proc. SPIE* **2009**, *7377*, 73770R.
(13) Xia, Z.; Riester, L.; Sheldon, B. W.; Curtin, W. A.; Liang, J.; Yin, A.; Xu, J. M. *Rev. Adv. Mater. Sci.* **2004**, *6*, 131−139.
(14) Su, Y.; Fei, G. T.; Zhang, Y.; Yan, P.; Li, H.; Shang, G. L.; Zhang, L. D. *Mater. Lett.* **2011**, *65*, 2693−2695.
(15) Wang, B.; Fei, G. T.; Wang, M.; Kong, M. G.; Zhang, L. D. *Nanotechnology* **2007**, *18*, 365601.
(16) Losic, D.; Lillo, M.; Losic, D., Jr. *Small* **2009**, *5*, 1392−1397.
(17) Lee, W.; Schwirn, K.; Steinhart, M.; Pippel, E.; Scholz, R.; Gösele, U. *Nat. Nanotechnol.* **2008**, *3*, 234−239.
(18) Zheng, W. J.; Fei, G. T.; Wang, B.; Jin, Z.; Zhang, L. D. *Mater. Lett.* **2009**, *63*, 706−708.
(19) Zheng, W. J.; Fei, G. T.; Wang, B.; Zhang, L. D. *Nanoscale Res. Lett.* **2009**, *4*, 665−667.
(20) Rahman, M. M.; Garcia-Caurel, E.; Santos, A.; Marsal, L. F.; Pallarès, J.; Ferré-Borrull, J. *Nanoscale Res. Lett.* **2012**, *7*, 474.
(21) Nielsch, K.; Choi, J.; Schwim, K.; Wehrspohn, R. B.; Gösele, U. *Nano Lett.* **2002**, *2*, 677−680.
(22) Ono, S.; Masuko, N. *Surf. Coat. Technol.* **2003**, *169−170*, 139−142.
(23) Santos, A.; Formentin, P.; Pallarès, J.; Ferré-Borrull, J.; Marsal, L. F. *Mater. Lett.* **2010**, *64*, 371−374.
(24) Brevnov, D.A.; Rao, G.V.R.; López, G. P.; Atanassov, P. B. *Electrochim. Acta* **2004**, *49*, 2487−2494.
(25) Aspnes, D. E; Theeten, J. B; Hottier, F. *Phys. Rev. B* **1979**, *20*, 3292−3302.
(26) Sakoda, K. *Optical Properties of Photonic Crystals*; Springer: New York, 2005; pp 23−26.